Asymptotic/Numerical Analysis of Supersonic Propeller Noise

M. K. Myers* and R. Wydeven†
George Washington University, Hampton, Virginia 23665

An asymptotic analysis based on the Mach surface structure of the field of a supersonic helical source distribution is applied to predict thickness and loading noise radiated by high-speed propeller blades. The theory utilizes an integral representation of the Ffowcs Williams-Hawkings equation in a fully linearized form. The asymptotic results are used for chordwise strips of the blade, whereas required spanwise integrations are performed numerically. The form of the analysis enables predicted waveforms to be interpreted in terms of Mach surface propagation. A computer code developed to implement the theory is described and found to yield results in close agreement with more exact computations.

Introduction

IN a previous paper,[1] an asymptotic analysis was developed to describe the acoustic field radiated by a chordwise distribution of sources moving supersonically along a helical path. The primary purpose of that work was to obtain a description of the field specifically related to the geometry of the Mach surfaces generated by the leading edge of the source distribution, which carry supersonic singularities away from the moving sources. The approximation developed is most accurate in regions close to the Mach surfaces. Because the amplitude of the disturbance is known to be much higher there than it is elsewhere in the field, it was expected that the asymptotic theory would be capable of producing reasonably accurate numerical predictions and could be a useful tool for acoustic analyses of high-speed propellers. In that context, however, the earlier work described only the thickness noise of a single chordwise strip of a supersonic blade. After the noise radiated by such a strip was calculated using the most recent and most accurate Farassat code,[2] it was found that the asymptotic results were surprisingly accurate and that they could be obtained with a substantially lower expenditure of computation time.

The current paper describes an application of the asymptotic method to the calculation of the noise of a complete high-speed propeller blade, including both the thickness and loading contributions. The analysis utilizes an integral representation of the solution to the Ffowcs Williams-Hawkings (FW-H) equation[3] in its fully linearized form. The required blade surface-time integrals are performed using the asymptotic approximation for the chord and time integrations with a subsequent numerical evaluation of the integral along the blade span; i.e., the blade is built up by superposing chordwise strips. A reasonably efficient computer code has been developed to implement the analysis. As before, the principal aim of the work is to construct a description of the radiated acoustic field that is directly linked to the structure of the Mach surfaces associated with the leading edge of the supersonic portion of the rotating blade. It will be seen that a number of aspects of the field such as waveform variations and spatial decay rates can be explained in the context of the structure and propagation of these surfaces. In addition, in view of the results found in Ref. 1, it is of interest to assess the potential of the asymptotic procedure to predict accurate numerical values when applied to a complete blade. Finally, it is of value to determine whether the new code can result in significant savings of computation time. If so, it could be useful as a preliminary tool to assess blade designs even if the code proved less accurate than others currently available.

The two major noise-prediction codes in common use are the Dunn-Farassat-Padula advanced turboprop (DFP-ATP) code[2,4] and the Hanson code.[5] The DFP-ATP code employs a time-domain analysis that starts from integral representations of the solution to the FW-H equation, whereas the Hanson code calculates the noise in the frequency domain. Both codes can be computationally expensive, the first because of the complex formulation it requires for supersonic blade panels, and the second because it must perform extensive evaluations of transcendental functions. These codes, of course, are known to produce comparable and accurate results; the DFP-ATP code is used as the standard in the current work with which to compare the predictions of the new approximate code.

Formal Integral Representation

Fully Linearized FW-H Equation

The asymptotic technique to be used in the following applies to a fully linearized or "mean surface" formulation of the boundary value problem governing the acoustic pressure generated in a stationary ideal fluid by a thin rigid body moving at velocity $\boldsymbol{V}$. Let the body surface S be defined by $f(\boldsymbol{x},t;\epsilon)=0$ such that $f>0$ exterior to S and $f<0$ interior to S. Here, ϵ is a small parameter characterizing the magnitude of the small perturbations the body is presumed to impart to the otherwise stationary fluid. The coordinate vector $\boldsymbol{x}$ is measured relative to a frame fixed in the undisturbed fluid. It follows that the unit outer normal $\boldsymbol{n}$ to the body and its normal velocity $V_n = \boldsymbol{V}\cdot\boldsymbol{n}$ are given by

$$|\nabla f| n_i = \frac{\partial f}{\partial x_i} \qquad |\nabla f| V_n = -\frac{\partial f}{\partial t} \tag{1}$$

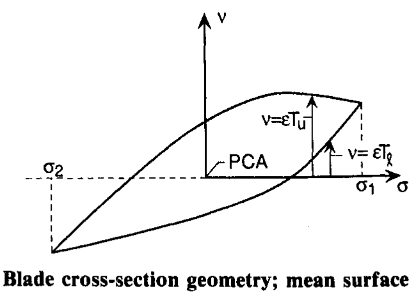

Fig. 1 Blade cross-section geometry; mean surface is $\nu = 0$.

Received Nov. 6, 1989; revision received May 23, 1990; accepted Aug. 1, 1990.

*Professor of Engineering and Applied Science, Joint Institute for Advancement of Flight Sciences; mailing address: MS 269, NASA Langley Research Center, Hampton, VA 23665. Associate Fellow AIAA.

†Research Assistant, Joint Institute for Advancement of Flight Sciences; currently at Bell Helicopter Textron, Ft. Worth, TX 76101. Student Member AIAA.

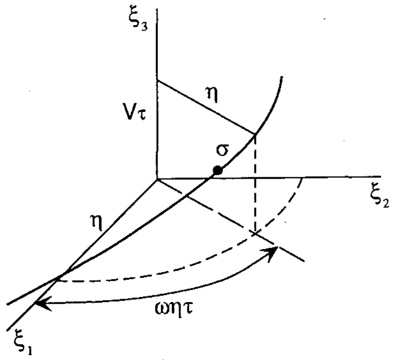

Fig. 2 Helical source path.

evaluated on $f = 0$. The small disturbance criterion $V_n/c \ll 1$, where c is the sound speed, is thus equivalent to the requirement that $\partial f/\partial t$ be $\mathcal{O}(\epsilon)$ in magnitude.

Let $\tilde{p}$ be defined according to

$$\tilde{p} = \begin{cases} p & f > 0 \\ 0 & f < 0 \end{cases}$$

where p is the acoustic pressure in the field exterior to S. Then $\tilde{p}$ is defined over all space and is discontinuous across S. The use of the concept of generalized differentiation in conjunction with the ideal fluid equations of motion then leads[6,7] to the FW-H equation

$$\bar{\square}^2\tilde{p} = \frac{1}{c^2}\frac{\bar{\partial}^2\tilde{p}}{\partial t^2} - \frac{\bar{\partial}^2\tilde{p}}{\partial x_i^2} = \frac{\bar{\partial}}{\partial t}[\rho_0 V_n|\nabla f|\delta(f)] - \frac{\bar{\partial}}{\partial x_i}[pn_i|\nabla f|\delta(f)] \tag{2}$$

in which ρ_0 is the ambient fluid density, the overbars denote generalized differentiation, and the nonlinear quadrupole term has been omitted from the right side. Equation (2) governs the discontinuous quantity $\tilde{p}$ over the entire three-dimensional space.

Because of the small disturbance requirement, the left side of Eq. (2) is $\mathcal{O}(\epsilon)$ in magnitude. The fully linearized version of the equation is derived by writing the right side in terms of a mean surface and then eliminating all contributions to it that are $\mathcal{O}(\epsilon^2)$ or smaller. Let the upper and lower surfaces of the blade be given by $f_u(\boldsymbol{x},t;\epsilon) = 0$ and $f_\ell(\boldsymbol{x},t;\epsilon) = 0$, respectively, such that for $\epsilon = 0$ both reduce to $f_m = 0$. The mean surface $f_m = 0$ is defined such that its normal velocity is everywhere zero, i.e., it moves only tangent to itself and does not disturb the ideal fluid. Thus, from Eq. (1), it follows that f_m is independent of t. Define $\nu(\boldsymbol{x})$ as the distance from the mean surface along its local normal direction. Note that $|\nabla\nu| = 1$. Then let f_u, f_l be written as

$$f_u(\boldsymbol{x},t;\epsilon) = \nu - \epsilon T_u(\boldsymbol{x},t) \tag{3a}$$

$$f_\ell(\boldsymbol{x},t;\epsilon) = -\nu + \epsilon T_\ell(\boldsymbol{x},t) \tag{3b}$$

so that T_u and T_ℓ describe the normal displacements of points on the upper and lower blade surfaces above the mean surface $f_m = \nu = 0$ (see Fig. 1). It follows from the definition of the Dirac delta function that each term on the right in Eq. (2) can be separated into two, one for the upper and one for the lower surface of the blade. For example,

$$V_n|\nabla f|\delta(f) = V_{nu}|\nabla f_u|\delta(f_u) + V_{n\ell}|\nabla f_\ell|\delta(f_\ell)$$

The use of Eqs. (1) and (3) results in

$$\boldsymbol{n}_u = \boldsymbol{n}_m + \mathcal{O}(\epsilon) \qquad \boldsymbol{n}_\ell = -\boldsymbol{n}_m + \mathcal{O}(\epsilon)$$

$$V_{nu} = -\epsilon\boldsymbol{V}\cdot\nabla T_u + \mathcal{O}(\epsilon) \qquad V_{n\ell} = \epsilon\boldsymbol{V}\cdot\nabla T_\ell + \mathcal{O}(\epsilon)$$

and because p itself is $\mathcal{O}(\epsilon)$ in magnitude,

$$p_u\boldsymbol{n}_u = p_u\boldsymbol{n}_m + \mathcal{O}(\epsilon) \qquad p_\ell\boldsymbol{n}_\ell = -p_\ell\boldsymbol{n}_m + 0(\epsilon)$$

where $\boldsymbol{n}_m = \nabla\nu$ is the unit vector to the mean surface pointing toward the upper or suction side of the blade. In addition, it is known that the delta function $\delta(f)$ may be considered formally to have a power series expansion in ϵ about $\epsilon = 0$[8] so that

$$\delta(f_{u,\ell}) = \delta(f_m) + \mathcal{O}(\epsilon)$$

Finally, all of these expressions are substituted into the separated form of the right side of Eq. (2) and all terms of $\mathcal{O}(\epsilon^2)$ are neglected. This yields what is termed here the fully linearized FW-H equation

$$\bar{\square}^2\tilde{p} = 2\frac{\bar{\partial}}{\partial t}[\rho_0\hat{V}_n\delta(f_m)] + \frac{\bar{\partial}}{\partial x_i}[\Delta p n_{m_i}\delta(f_m)] \tag{4}$$

in which $\Delta p = p_\ell - p_u$ and $\hat{V}_n$ is given by

$$2\hat{V}_n = -\epsilon\boldsymbol{V}\cdot(\nabla T_u - \nabla T_\ell) \tag{5}$$

That is, $\hat{V}_n$ is the average of the normal velocities of the upper and lower sides of the blade. Equation (4) is the desired result and is the governing equation on the quantity $\tilde{p}$ that will be analyzed in the remainder of this work. As is common, it is conveniently split into two parts according to

$$\bar{\square}^2\tilde{p}_T = 2\frac{\bar{\partial}}{\partial t}[\rho_0\hat{V}_n\delta(f_m)] \tag{6a}$$

$$\bar{\square}^2\tilde{p}_L = \frac{\bar{\partial}}{\partial x_i}[\Delta p n_{m_i}\delta(f_m)] \tag{6b}$$

where the subscripts T and L denote thickness noise and loading noise, respectively. The representation of $\tilde{p}_T$ and $\tilde{p}_L$ that follows from solving Eqs. (6) using the free-space Green's function is discussed in the following section.

Solution of the FW-H Equation

Solutions of Eqs. (6) can be derived by considering an equation of the form

$$\bar{\square}^2\Phi = Q(\boldsymbol{x},t)\,\delta[f_m(\boldsymbol{x})] \tag{7}$$

which holds over all of space. The formal solution to Eq. (6) can be obtained using the free-space Green's function for the wave operator in the form of the four-dimensional integral

$$\Phi(\boldsymbol{x},t) = \frac{1}{4\pi}\int\frac{Q(\boldsymbol{\xi},\tau)}{r(\boldsymbol{x},\boldsymbol{\xi})}\delta[f_m(\boldsymbol{\xi})]\delta[g(\boldsymbol{x},t;\boldsymbol{\xi},\tau)]\,\mathrm{d}\boldsymbol{\xi}\,\mathrm{d}\tau \tag{8a}$$

$$g = t - \tau - \frac{r}{c} \qquad r = |\boldsymbol{x} - \boldsymbol{\xi}| \tag{8b}$$

Now new Cartesian source coordinates $\boldsymbol{\xi}'$ measured in a frame of reference fixed to the moving rigid body are introduced, and it is assumed that Q is independent of time in the body-fixed frame. The Jacobian of the transformation $\boldsymbol{\xi}\rightarrow\boldsymbol{\xi}'$ is unity. In addition,[6]

$$\mathrm{d}\boldsymbol{\xi}' = \frac{\mathrm{d}\xi_1'\,\mathrm{d}\xi_2'|\nabla f_m|}{|\partial f_m/\partial\xi_3'|}\frac{\mathrm{d}f_m}{|\nabla f_m|} = \mathrm{d}S\frac{\mathrm{d}f_m}{|\nabla f_m|} = \mathrm{d}S\,\mathrm{d}f_m$$

where $\mathrm{d}S$ is the area element on the surface $f_m = 0$. This allows an integration over f_m to be carried out in Eqs. (8) and puts it in the form

$$\Phi(\boldsymbol{x},t) = \frac{1}{4\tau}\int\frac{Q}{r}\delta(g)\,\mathrm{d}S\,\mathrm{d}\tau \tag{9}$$

in which Q, r, and g are now functions of ξ' and are evaluated on the mean surface.

In order to utilize these results for Eq. (6b), it is noted that

$$\frac{\partial \Phi}{\partial x_i} = \frac{1}{4\pi}\int Q \frac{\partial}{\partial x_i}\left[\frac{\delta(g)}{r}\right] \mathrm{d}S\, \mathrm{d}\tau \tag{10}$$

which can be rewritten in terms of a time derivative by use of the relation[6]

$$\frac{\partial}{\partial x_i}\left[\frac{\delta(g)}{r}\right] = \frac{1}{c}\frac{\partial}{\partial t}\left[\frac{\hat{r}_{mi}\delta(g)}{r}\right] - \frac{\hat{r}_{mi}\delta(g)}{r^2}$$

Here $\hat{r}_m$ is a unit vector in the direction of radiation from the mean surface. Thus, Eq. (10) is equivalent to

$$\frac{\partial \Phi}{\partial x_i} = -\frac{1}{4\pi c}\frac{\partial}{\partial t}\int \frac{Q\hat{r}_{mi}}{r}\delta(g)\, \mathrm{d}S\, \mathrm{d}\tau - \frac{1}{4\pi}\int \frac{Q\hat{r}_{mi}}{r^2}\delta(g)\, \mathrm{d}S\, \mathrm{d}\tau \tag{11}$$

Finally, the solutions to Eqs. (6) are expressed using Eqs. (9) and (11) as

$$\tilde{p}_T = \frac{\rho_0}{2\pi}\frac{\partial}{\partial t}\int \frac{\hat{V}_n}{r}\delta(g)\, \mathrm{d}S\, \mathrm{d}\tau \tag{12}$$

$$\tilde{p}_L = -\frac{1}{4\pi c}\frac{\partial}{\partial t}\int \frac{\Delta p \cos\theta}{r^2}\delta(g)\, \mathrm{d}S\, \mathrm{d}\tau - \frac{1}{4\pi}\int \frac{\Delta p \cos\theta}{r^2}\delta(g)\, \mathrm{d}S\, \mathrm{d}\tau \tag{13}$$

in which $\cos\theta = n_{mi}\,\hat{r}_{mi}$; θ is the angle between the normal to the mean surface and the radiation direction from the mean surface. Again, it is emphasized that each integrand in Eqs. (12) and (13) is considered a function of ξ' and τ and is evaluated on the mean surface $f_m = 0$. Equations (12) and (13) are the final integral representations of the fully linearized thickness and loading pressures that are used in this work.

Mach Surface Structure

The following analysis relies heavily on the detailed structure of the Mach surface generated by the leading edge of a supersonic propeller blade. Much can be learned about this structure by considering a single point source transversing its path supersonically. Since this was discussed at some length in Ref. 1, a relatively brief review is presented here.

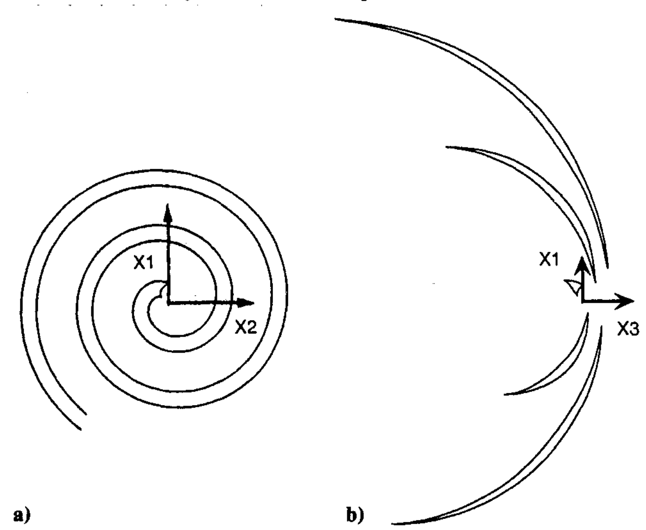

Fig. 3 Source Mach envelope in translating frame: a) In plane of rotation; b) Normal to plane of rotation.

The elementary signal emitted by a source at time $\tau \leq t$ propagates into space within a spherical wavefront centered at the emission point $\xi(\tau)$ and of radius

$$r(\tau) = |r(\tau)| = |x - \xi(\tau)| = c(t - \tau) \tag{14}$$

where c is the speed of sound. The Mach surface associated with the source is the envelope of all these spheres over all emission times τ. It is obtained by solving Eq. (14) simultaneously with its derivative with respect to τ:

$$\frac{\partial r}{\partial \tau} = -c \qquad \text{or} \qquad \frac{r}{r}\cdot\frac{\mathrm{d}\xi}{\mathrm{d}\tau} = c \tag{15}$$

Note that Eq. (15) implies that only signals emitted during supersonic portions of the source motion contribute to the envelope.

Suppose the source is moving at constant speed in the direction of increasing ξ_3 along the helical path illustrated in Fig. 2. The Cartesian coordinates of the source are

$$\xi_1 = \eta \cos\omega\left(\tau - \frac{\sigma}{V_h}\right)$$
$$\xi_2 = \eta \sin\omega\left(\tau - \frac{\sigma}{V_h}\right)$$
$$\xi_3 = V_f\left(\tau - \frac{\sigma}{V_h}\right) \tag{16}$$

in which V_f is the forward speed and η is the constant radius of the helix. The translating and rotating radius along which η is measured is the pitch change axis (PCA) when the source is considered to represent an element of a propeller blade. In Eq. (16), σ is the distance along the helical source path from the PCA to the source measured positive in the direction of decreasing ξ_3. Finally, V_h is the helical speed:

$$V_h = (V_f^2 + \omega^2\eta^2)^{1/2} > c \tag{17}$$

Figure 3 depicts the Mach envelope for a source moving according to Eq. (16) plotted in a frame of reference $X = (x_1, x_2, x_3 - V_f t)$ translating with the hub of the rotating source. In this frame, the source revolves about the x_3 axis in the (X_1, X_2) plane. Shown are the intersections of the Mach surface with the plane of rotation of the source in Fig. 3a and with the meridian plane $X_2 = 0$ in Fig. 3b. The structure shown is typical of cases for which the forward speed is subsonic; here, $V_f/c = 0.94$ and $V_h/c = 1.23$. It is evident that the envelope is a closed, spiral surface that has a crescent-shaped cross section whose width increases away from the rotation axis. The two branches of the coiled surface meet at cusps at each edge. The locus of the cusps as the spiral expands outward is a caustic surface of the orthogonal trajectories of the envelope that are known as rays. Every ray is tangent to the caustic surface, and no rays penetrate the region outside it. The caustic surface itself is given by the simultaneous solution of Eqs. (14) and (15) with the derivative of Eq. (15) with respect to τ:

$$\frac{\partial^2 r}{\partial \tau^2} = \frac{V_h^2 - c^2}{r} - \frac{r}{r}\cdot\frac{\mathrm{d}^2\xi}{\mathrm{d}\tau^2} = 0 \tag{18}$$

As in Ref. 1, this can be shown to yield the hyperboloid of revolution illustrated in the translating reference frame in Fig. 4. In geometric acoustic terminology, the region interior to the caustic is said to be illuminated, whereas that exterior to it is said to be in an acoustic shadow. It is known generally, and from Ref. 1 in particular, that the major acoustic disturbance in the field is confined to the interior of the Mach surface, i.e., inside the crescent-shaped cells of Fig. 3b. In addition, the caustic represents a partial focus of the disturbance, and amplitudes experienced at a point near it as a cell passes are

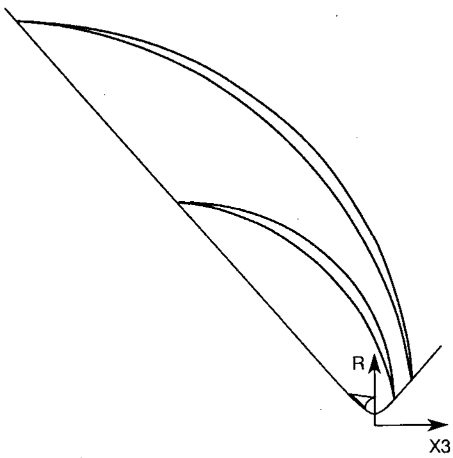

Fig. 4 Caustic surface in translating frame.

significantly higher than those farther interior to the illuminated zone.

Now, each point of a propeller blade can be regarded as imparting a point disturbance to the fluid that has a Mach envelope structure of the aforementioned form associated with it. The leading edge of the blade establishes the overall wavefront upon which the asymptotic treatment of Eqs. (12) and (13) will be based. Just as for the corresponding problem of a wing in uniform supersonic motion (for which the individual point source envelopes are the familiar Mach cones), a supersonic leading edge yields an overall wavefront that is itself the envelope of individual Mach surfaces. On the other hand, a subsonic leading edge causes individual fronts to be offset such that cumulative strengthening of the field, which occurs for nonswept leading edges, is reduced. In the current work, the integration over the blade span required in Eqs. (12) and (13) is performed numerically, and no detailed illustrations of the geometry of Mach surfaces corresponding to spanwise distributions of sources along a leading edge will be given. The reader is directed to Ref. 9, in which more discussion of these composite Mach surfaces appears.

Asymptotic Approximation

To proceed with the evaluation of $\tilde{p}$ using Eqs. (12) and (13), Eq. (9) will again be considered. Mean surface coordinates on $f_m = 0$ are taken to be σ and η as defined in Eq. (16); the mean surface area element dS is $d\sigma\, d\eta$. Then Eq. (9) is

$$4\pi\Phi = \int_{\eta_1}^{\eta_2}\int_{-\infty}^{t}\int_{\sigma_1}^{\sigma_2} \frac{Q(\sigma,\eta)}{r(\boldsymbol{x},\sigma,\eta,\tau)}\, \delta[g(\boldsymbol{x},t;\sigma,\eta,\tau)]\, d\sigma\, d\tau\, d\eta \tag{19}$$

Here g is as defined in Eq. (8b) and

$$r = |\boldsymbol{x} - \boldsymbol{\xi}(\sigma,\eta,\tau)|$$

with $\boldsymbol{\xi}$ given by Eq. (16). The chordwise positions of the leading and trailing edges of the blade mean surface are denoted σ_1 and σ_2, respectively (see Fig. 1), and η_1 and η_2 are its inner and outer spanwise limits. Then the inner double integral in Eq. (19) gives the field of a chordwise distribution of sources representing a single constant-η blade strip of width $d\eta$. It is precisely of the form treated in Ref. 1:

$$\phi(\boldsymbol{x},t,\eta) = \int_{-\infty}^{t}\int_{\sigma_1}^{\sigma_2} \frac{Q(\sigma)}{r(\sigma,\tau)}\, \delta[g(\sigma,\tau)]\, d\sigma\, d\tau \tag{20}$$

where the dependence of the terms in the integrand on $\boldsymbol{x}$ and η is temporarily suppressed.

The function $g = t - \tau - r(\sigma,\tau)/c$ is the key to the following development. It establishes the phase of the wave system emitted by the source located at chord position σ over its emission times τ. It is known[1] that for helicoidal supersonic source motion, g behaves in τ in a manner similar to a cubic function; i.e., it has two stationary points $\tau = \hat{s}_\pm$ that satisfy

$$g_\tau = -1 - r_\tau(\sigma,\hat{s}_\pm)/c = 0 \tag{21}$$

in which the subscript notation is used to indicate differentiation with respect to τ. Reference to Eq. (15) shows that $\hat{s}_\pm(\sigma)$ are the emission times of the two elementary signals emitted by the source at σ that carry the Mach envelope associated with that source. That is, $\hat{s}_\pm$ define the rays from the source path to each branch of the envelope cells depicted in Fig. 3b that pass through a given observer point at $\boldsymbol{x}$. The corresponding values $g(\sigma,\hat{s}_\pm)$ measure the time elapsed after the arrival of the envelope branches at $\boldsymbol{x}$. For subsonic motion, or for any $\boldsymbol{x}$ exterior to the caustic surface, real rays do not exist. In this case, the stationary points $\hat{s}_\pm$ are complex conjugates. At the cusps on the envelope, $g_{\tau\tau} = -r_{\tau\tau}/c = 0$ by Eq. (18). Therefore, the two stationary points coalesce for $\boldsymbol{x}$ on the caustic surface itself so that $\hat{s}_+ = \hat{s}_- = \hat{s}_*$.

Now when Eq. (16) is used in r, it is found that τ appears only in the combination $\tau - \sigma/V_h$. Thus, it follows that $\hat{s}_\pm(\sigma) - \sigma/V_h = = \hat{s}_\pm(\sigma_1) - \sigma_1/V_h$, or

$$\hat{s}_\pm(\sigma) = s_\pm + (\sigma - \sigma_1)/V_h \tag{22a}$$

where the definition $s_\pm = \hat{s}_\pm(\sigma_1)$ has been introduced. For the same reason, it follows that

$$\boldsymbol{r}[\sigma,\hat{s}_\pm(\sigma)] = \boldsymbol{r}(\sigma_1,s_\pm) \equiv \boldsymbol{R}_\pm \tag{22b}$$

$$g[\sigma,\hat{s}_\pm(\sigma)] = g(\sigma_1,s_\pm) - (\sigma - \sigma_1)/V_h$$
$$\equiv T_\pm - (\sigma - \sigma_1)/V_h \tag{22c}$$

Therefore, the Mach surface structure associated with any point σ on the strip is characterized entirely by that associated

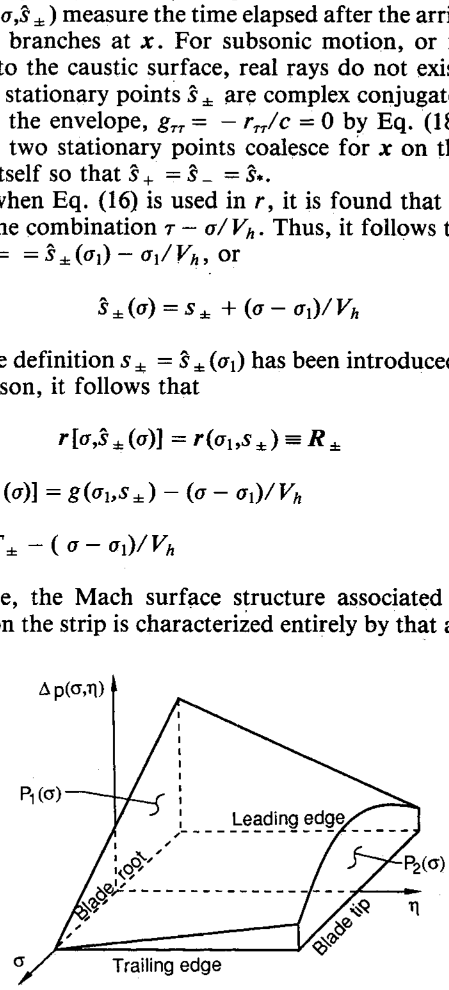

Fig. 5 Model loading distribution.

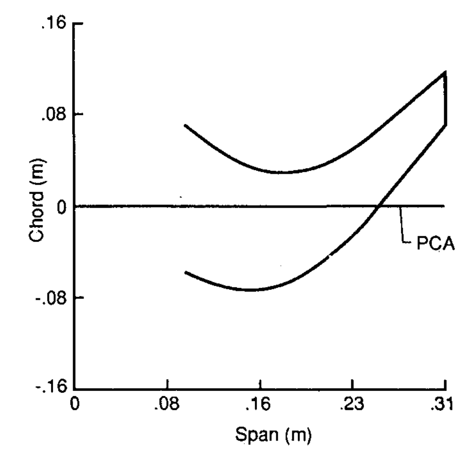

Fig. 6 Model mean surface planform.

with the leading edge $\sigma = \sigma_1$. The quantities $T_\pm = t - s_\pm - R_\pm/c$ are the elapsed times since the arrival of the two branches of the leading-edge envelope at $\boldsymbol{x}$.

The behavior of $g(\sigma,\tau)$ suggests a cubic transformation $\tau \rightarrow u$ defined by

$$g(\sigma,\tau) = \hat{A} + Bu - u^3/3$$

such that

$$g_\tau = (B - u^2)u_\tau$$

It follows from Eq. (21) that if u is chosen such that $u = \pm B^{1/2}$ when $\tau = \hat{s}_\pm$, then $u_\tau \neq 0$. In addition,

$$\hat{A} = [g(\sigma,\hat{s}_+) + g(\sigma,\hat{s}_-)]/2$$

$$B = \{3[g(\sigma,\hat{s}_+) - g(\sigma,\hat{s}_-)]/4\}^{2/3}$$

Note that, from the definition of g,

$$\begin{aligned}\hat{A} &= t - (s_+ + s_-)/2 - (R_+ + R_-)/2c - (\sigma - \sigma_1)/V_h \\ &\equiv A - (\sigma - \sigma_1)/V_h \end{aligned} \tag{23}$$

and that B is independent of t. Substitution of the transformation $\tau \rightarrow u$ into Eq. (20) yields

$$\phi = \int_u \int_{\sigma_1}^{\sigma_2} Q(\sigma)\, h(\sigma,u)\, \delta\left(\hat{A} + Bu - \frac{u^3}{3}\right) \mathrm{d}\sigma\, \mathrm{d}u \tag{24}$$

in which

$$h(\sigma,u) = \frac{1}{r|\partial u/\partial\tau|} = \frac{B - u^2}{r|g_\tau|} \tag{25}$$

Because $u_\tau \neq 0$, h is a regular function of u; it is written as

$$h(\sigma,u) = h_0 + uh_1 + (B - u^2)\bar{h}(\sigma,u)$$

from which it follows that

$$h_0 = \frac{[h(\sigma,B^{1/2}) + h(\sigma, -B^{1/2})]}{2}$$

$$h_1 = \frac{[h(\sigma,B^{1/2}) - h(\sigma, -B^{1/2})]}{2} \tag{26}$$

and because $h(\sigma, \pm B^{1/2})$ involves only $r[\sigma,\hat{s}_\pm(\sigma)]$, both h_0 and h_1 are independent of σ. This allows Eq. (24) to be put into the form

$$\begin{aligned}\phi &= h_0 \int_u \int_{\sigma_1}^{\sigma_2} Q\delta\left(\hat{A} + Bu - \frac{u^3}{3}\right) \mathrm{d}\sigma\, \mathrm{d}u \\ &+ h_1 \int_u \int_{\sigma_1}^{\sigma_2} uQ\delta\left(\hat{A} + Bu - \frac{u^3}{3}\right) \mathrm{d}\sigma\, \mathrm{d}u \\ &+ \int_u \int_{\sigma_1}^{\sigma_2} Q\bar{h}\delta\left(\hat{A} + Bu - \frac{u^3}{3}\right)(B - u^2)\, \mathrm{d}\sigma\, \mathrm{d}u \end{aligned} \tag{27}$$

As shown in Ref. 1, an integration by parts on the third member of Eq. (27) results in the conclusion that it is negligible compared to the others, provided that $|cT_\pm/R_\pm| \ll 1$. This is true if the observer point $\boldsymbol{x}$ is sufficiently close to the Mach envelope associated with the leading edge of the blade strip. Finally, the asymptotic approximation to Eq. (27) is obtained by neglecting the third term. The use of Eq. (23) allows the integral over σ to be performed explicitly, and the approximation becomes

$$\phi(\boldsymbol{x},t,\eta) = h_0 V_h \int_u Q[z(u)]\, \mathrm{d}u + h_1 V_h \int_u uQ[z(u)]\, \mathrm{d}u \tag{28}$$

Here $z(u) = V_h(A + \sigma_1/V_h + Bu - u^3/3)$ and the limits on the u integration are such that

$$\sigma_1 \leq z(u) \leq \sigma_2 \tag{29}$$

In general, several such ranges of u exist; the integration in Eq. (28) must be done over each and the results summed to obtain ϕ.

The coefficients h_0 and h_1 are defined by Eq. (26). As shown in Ref. 1, $h(\sigma, \pm B^{1/2})$ can be written explicitly for $B \neq 0$ as

$$h(\sigma, \pm B^{1/2}) = \left[\frac{2B^{1/2}}{\pm(c\beta^2 R_\pm - \dot{M}_{R_\pm} R_\pm^2)}\right]^{1/2}$$

and for $B = 0$ (on the caustic of the leading-edge envelope) as

$$h(\sigma,0) = \left[\frac{-2}{\dot{M}_{R_*} R_*^3}\right]^{1/3}$$

Here $\beta^2 = M^2 - 1$, $R_* = r(\sigma_1,s^*)$, and $\dot{M}_{R_\pm}$ and $\dot{M}_{R_*}$ are the components of $\dot{\boldsymbol{M}}$ and $\dot{\boldsymbol{M}}$ in the directions of $\boldsymbol{R}_\pm$ and $\boldsymbol{R}_*$. $\boldsymbol{M}$ is the blade Mach number.

One further step is necessary to utilize these results in evaluating Eqs. (12) and (13). These require terms of the form

$$\frac{\partial\bar{\Phi}}{\partial t} = \frac{1}{4\pi}\int_{\eta_2}^{\eta_1} \frac{\partial\phi}{\partial t}\, \mathrm{d}\eta \tag{30}$$

The time derivative of ϕ is easily calculated because only the limits in Eq. (28) and the A in the argument of $z(u)$ contain t. By using Eq. (23) and considering just the first term of Eq. (28), it follows that $\partial\phi/\partial t$ takes the form

$$\begin{aligned}\frac{\partial\phi}{\partial t} &= h_0 V_h^2 \int_{u_0}^{u_1} Q'[z(u)]\, \mathrm{d}u \\ &+ h_0 V_h Q[z(u_0)]\frac{\partial u_1}{\partial t} - h_0 V_h Q[z(u_0)]\frac{\partial u_0}{\partial t}\end{aligned} \tag{31}$$

in which the prime denotes differentiation with respect to the argument σ; a similar expression holds for the second term of Eq. (28). The terms $\partial u_{0,1}/\partial t$ follow by setting $z(u) = \sigma_1$ or σ_2 and differentiating; for example,

$$\frac{\partial\sigma_2}{\partial t} = \frac{\partial}{\partial t}\left[V_h\left(A + \frac{\sigma_1}{V_h} + Bu_1 - \frac{u_1^3}{3}\right)\right] = 0$$

which yields $\partial u_{0,1}/\partial t = -1/(B - u_{0,1}^2)$. There is one expression like Eq. (31) for each of the ranges $u_0 \leq u \leq u_1$ over which the inequality (29) is satisfied.

The asymptotic approximation embodied in Eqs. (28) and (31) represents the main theoretical result of the current work. Each of Eqs. (12) and (13) is in the form of Eq. (19) or (30), and it remains simply to substitute the appropriate integrands and to carry out the integration over the spanwise variable η. For the thickness noise, Eq. (31) is used with $Q = \hat{V}_n(\sigma,n)$. For the first term of Eq. (13), Eq. (31) is used with $Q = \Delta p(\sigma,n)$ and the function h of Eq. (25) redefined to include the factor $\cos\theta$. The second term of Eq. (31) is treated using Eq. (28) with $Q = \Delta p$ and with h incorporating an additional factor of $1/r$. Because the integration over η will be evaluated numerically and the full expressions for $\bar{p}_T$ and $\bar{p}_L$ are very lengthy, they will not be written out here; they can be found in Ref. 9. In the following section, the numerical evaluation of the asymptotic approximation of these quantities will be discussed.

Numerical Implementation

As mentioned, a computer code has been developed by the authors to evaluate the results of the asymptotic theory presented in the preceding section. A good deal of specific information about the code is given in Ref. 9; in the current paper, it will be described more briefly. The noise calculations are performed for an observer fixed in the translating reference frame X in which the disturbances are periodic with period $2\pi/\omega$.

Blade Data

In any application, the normal velocity $\hat{V}_n$ is known once the blade thickness distribution is given, and the loading Δp would be determined from measured or otherwise computed aerodynamic data. Here a model blade is defined along with a fictitious Δp distribution that is roughly representative of those known for actual blades.[2]

From Eq. (5) it follows that

$$2\hat{V}_n = \frac{\epsilon V_h \partial(T_u - T_\ell)}{\partial\sigma}$$

where $\epsilon(T_u - T_\ell)$ is the total thickness of the blade measured normal to the mean surface as previously defined. For the current calculations, this total thickness is assumed to have a biconvex parabolic distribution over $\sigma_1 \leq \sigma \leq \sigma_2$ with a thickness ratio that decreases linearly over the span $\eta_1 \leq \eta \leq \eta_2$. The Δp distribution assumed to act on the blade is illustrated schematically in Fig. 5. At the blade root it is linear, $P_1(\sigma)$, whereas at the tip it is a symmetric parabola, $P_2(\sigma)$, with a leading- and trailing-edge jump. The magnitude of the leading-edge jump at the tip is set equal to that corresponding to a supersonic airfoil at a 3 deg angle of attack and speed $V_h(\eta_2)$; the jump at the root increases to five times this value. The Δp distribution is then constructed using

$$\Delta p = \frac{\eta_2 - \eta}{\eta_2 - \eta_1} P_1(\sigma) + \frac{\eta - \eta_1}{\eta_2 - \eta_1} P_2(\sigma)$$

In addition, the mean surface planform is specified as depicted in Fig. 6. Other data used for all current computations are as listed in Table 1. These data correspond to a forward Mach number of 0.8 and a helical tip Mach number of 1.215.

Spanwise Integration

The pressures from Eqs. (12) and (13) are calculated using a Gauss-Legendre quadrature for the integration over the span variable η. The blade is divided into subintervals of width $\Delta\eta_j$ and one period $0 \leq \omega t \leq 2\pi$ is considered. At each η_k of a Gaussian distribution of span positions within the subinterval, the appropriate contributions from Eqs. (28) and (31) are evaluated over the entire period of observer time. These $\Delta P_j(\eta_k, t)$ are then multiplied by the required weighting factors w_k and summed to obtain the subinterval strip contribution to the blade pressure field. Finally, after repeating the the process for all subintervals along the span, the total blade pressure is constructed by summing over the strips:

$$p(X,t) = \sum_j \sum_k \Delta P_j(\eta_k, t) w_k \Delta\eta_j$$

Chord-Time Integration

The approximations expressed in Eqs. (28) and (31) are used at each η_k along the span, and the integrals over the variable u are evaluated using a substantially refined version of the procedure described in Ref. 1. The primary task is to calculate the stationary points $s_\pm$, which depend on t in the translating reference frame. For a given (X,t), A, B, h_0, and h_1 are simply calculated once $s_\pm$ are known. If at t the observer is within the caustic surface associated with $\sigma_1(\eta_k)$, then s_+ and s_- are real and $B > 0$. If the observer is outside the caustic, s_+ and s_- are complex conjugates and $B < 0$. However, from Eqs. (23) and (26), A, h_0, and h_1 are still real. Also, with $s_\pm$ known, the required sets of limits $u_{0,1}$ are found analytically using Cardan's formula to solve the cubic equations $z(u) = \sigma_1$ and $z(u) = \sigma_2$. The u integrations are then performed numerically.

The most troublesome task connected with the current method is to determine the points $s_\pm$ associated with each $\sigma_1(\eta_k)$ at each time t that satisfy Eq. (21). These are found in the code using Newton's method, which is efficient and accurate so long as suitable guesses for the roots can be made. Difficulties arise as a result of the fact that the translating observer can be both inside and outside the caustic during one period of time. The corresponding transitions between real and complex conjugate stationary points and vice versa necessitate a rather complex system of checks and adjustments for the method to converge successfully. The procedure developed, in which all checks and adjustments are done automatically in the program, has been tested extensively and found to be reliable. It is described in detail in Ref. 9. Calculation of the stationary points requires about 20% of the total computation time.

Table 1 Data for computations

Tip radius, m	0.312
Root radius, m	0.0936
Thickness ratio, tip	0.02
Thickness ratio, root	0.06
Chord/tip radius, tip	0.142
Chord/tip radius, root	0.4
Blade sweep at tip, deg	51.6
Angular speed, rad/s	884.33
Forward speed, m/s	241.2
Sound speed m/s	301.5
Air density, kg/m^3	0.457

Results and Discussion

Approximate predictions of thickness and loading noise using the current theory for the model blade have been checked extensively against those obtained from the DFP-ATP code applied to a closely similar blade. In the DFP-ATP code, data are specified on the actual blade surface and the chordwise variable is measured on a straight line normal to the PCA rather than along the helix of constant η. Whereas the mean surface formulation is easily simulated in that code, no simple correction can be made to account for the differing chord variable. Thus, the blades modeled in the two codes are not absolutely identical. It is known that small differences of this sort have very little effect on the overall character of the pressure signatures given by the DFP-ATP code, except that they can cause variations in details such as peak heights. As a result, calculations of pressure spectra were also carried out to assess the accuracy of the asymptotic theory at reproducing the practically important first several harmonics.

Figure 7 depicts two typical results. Here the observer is 4 blade radii out from the hub in the disk plane in Fig. 7a and 1 blade radius ahead of it in Fig. 7b. It is clear that the new theory produces waveforms that match very closely those of the more exact predictions, the major difference being a 5 to 10% error in peak magnitudes. As mentioned, these are most likely a result of slight differences in blade specification between the two analyses. The slope discontinuity and abrupt small pressure rise that occur early in the loading noise waveform appear to be caused by the large jump in Δp (Fig. 5) on the inboard leading edge, where the asymptotic strip results begin to lose accuracy because the helical speed is well below sonic. The spectra of each waveform, calculated using a standard fast Fourier transform routine, also can be seen to agree closely. In these and other causes, the first 7 to 8 harmonics are virtually identical and differences of only 2 to 3 dB exist out to 15 or more harmonics. Such illustrations of consistent agreement between the approximate and the DFP-ATP results indicate that the asymptotic theory and the new code are indeed accurate enough to be of value in supersonic blade noise prediction.

The time required by the new code to produce results like those of Fig. 7 is generally 50–75% of that needed to run the DFP-ATP code at its recommended default resolution parameter values.[4] This is a somewhat smaller time benefit than was originally anticipated from the single-strip comparisons noted in the Introduction. There are several relevant points to consider in this context. First, the efficiency of the new code is no doubt far from optimal. More important, however, obtaining the relatively smooth waveforms shown in Fig. 7 requires a very fine spanwise resolution. Individual strip contributions contain sharp, narrow spikes that vary quite rapidly both in magnitude and arrival time with span position so that summing over a coarse distribution of strips yields a blade waveform with many spurious sharp peaks. Since these have little influence on the lower harmonics, sufficiently accurate spectra could probably be obtained in much less than the time needed for those of Fig. 7. Moreover, the DFP-ATP code uses the time-consuming collapsing sphere analysis[2,4] only when necessary to handle blade panels moving at transonic-supersonic speed toward the observer. The new code utilizes the asymptotic strip analysis, which is the counterpart of the collapsing sphere method, over the entire blade. It would be significantly faster if it were combined with a simple retarded time solution for the subsonic part of the blade, as is done in Ref. 4.

Finally, Fig. 8 is included as a representative example of waveforms found using the current theory and to illustrate the

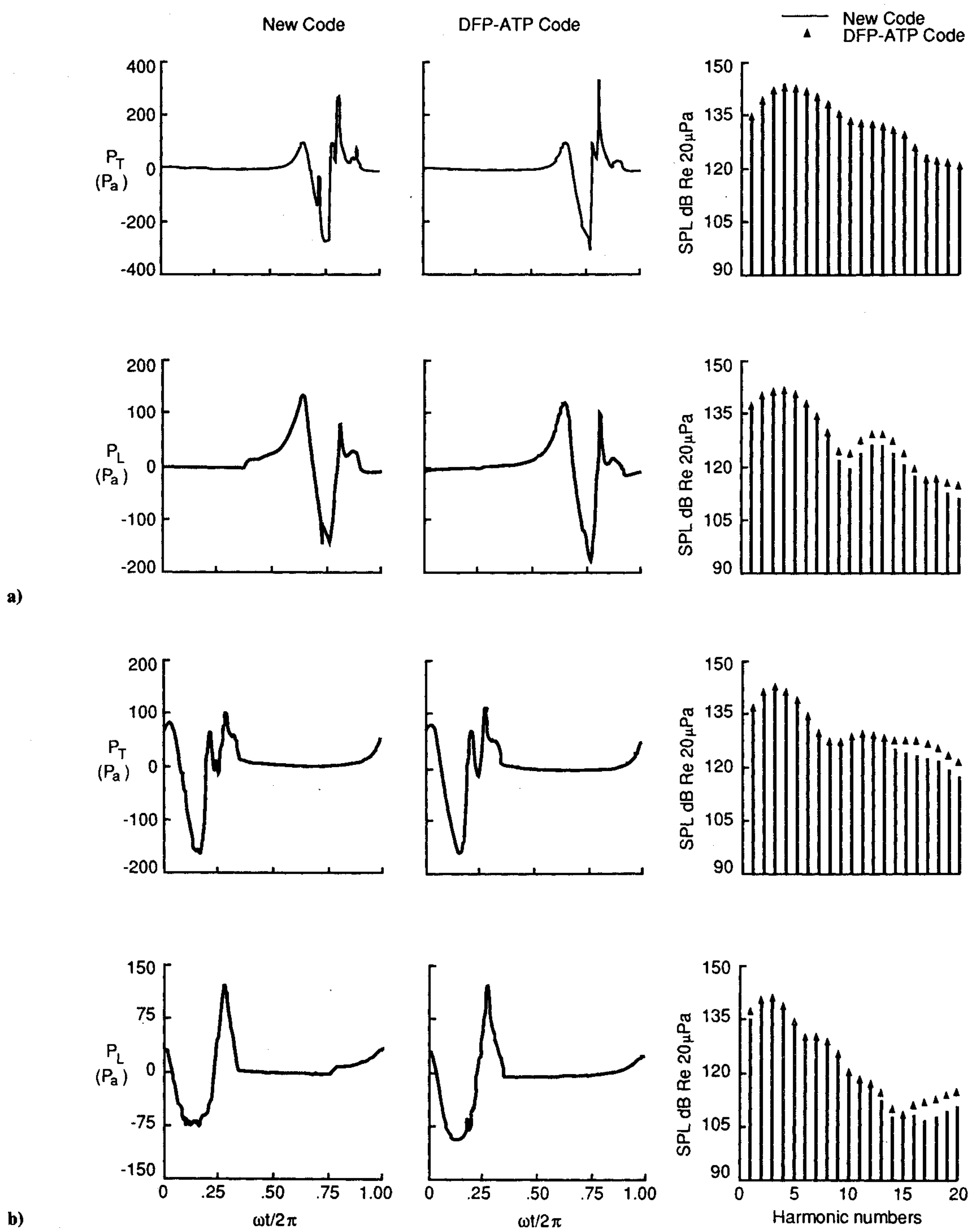

Fig. 7 Thickness and loading noise waveforms 4 blade radii out from the axis of rotation: a) In disk plane: $X = (1.248\ \mathrm{m}, 0, 0)$; b) 1 blade radius ahead of disk plane: $X = (1.248\ \mathrm{m}, 0, 0.312\ \mathrm{m})$.

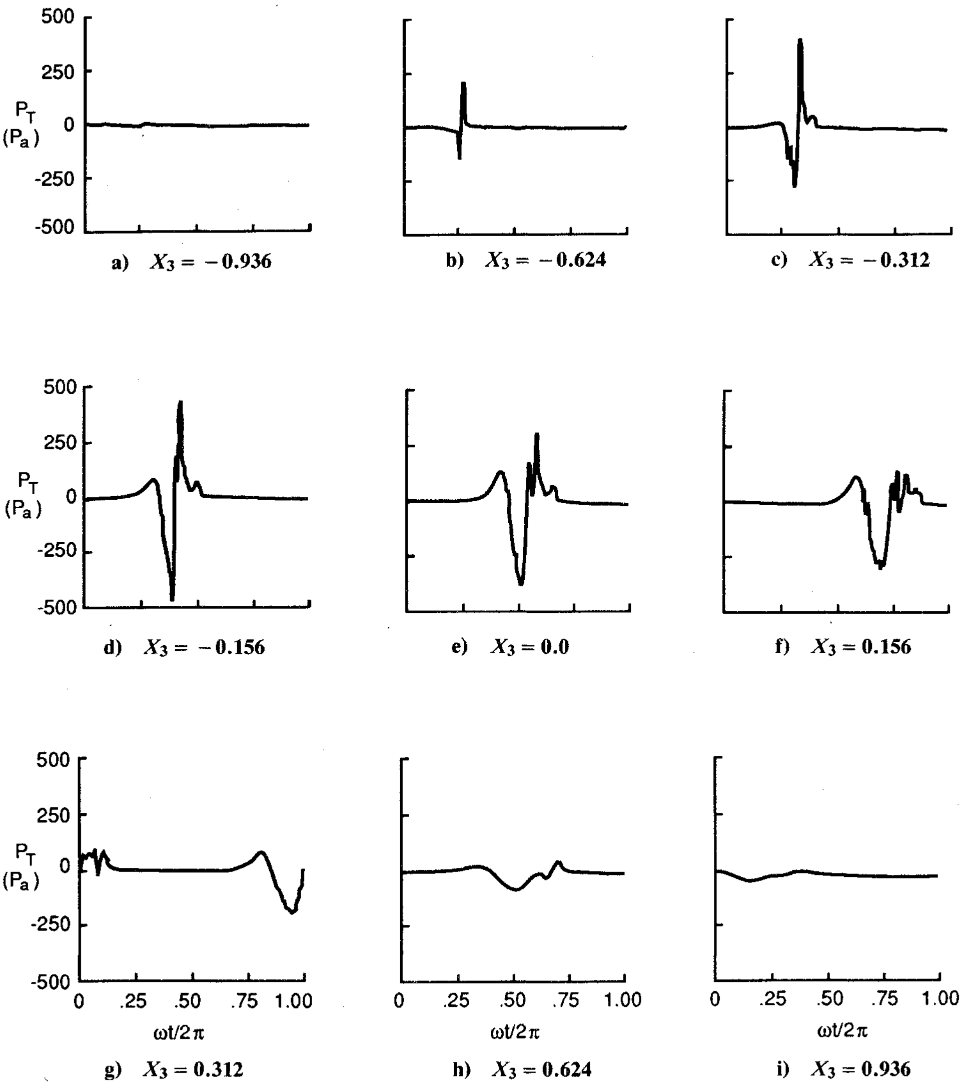

Fig. 8 Thickness noise waveforms from asymptotic theory along the line parallel to the axis of rotation: $X_1 = 0.936$ m, $X_2 = 0$.

fact that the asymptotic theory can provide insight into the behavior of these waveforms that is not easily obtained from the DFP-ATP code. Here the observer is at 3 blade radii from the hub and ½, 1, 2, and 3 radii behind and ahead of the disk plane. Only thickness noise is shown, but the loading noise signatures behave similarly.[9] Away from the disk plane, the signature shape changes substantially and in a manner completely consistent with the behavior predicted in Ref. 1 for single chordwise strip contributions of the form of Eqs. (28) and (31). It is known[1] that each individual chordwise strip creates a disturbance whose amplitude is enhanced for an observer near its associated caustic, especially the rear branch, at the time of passage of its Mach wavefront. Outside the caustic the amplitude drops rapidly to negligible values. Also, the signal width from each strip tends to narrow significantly at points behind the disk plane. These features are evident also in the results for the entire blade, which can be regarded as having associated with it a continuous distribution of single-strip caustics. Note that the disturbance amplitude in Fig. 8 increases and the signal width decreases behind the disk plane, although the somewhat weaker relative focusing found forward of this plane in Ref. 1 appears to be nearly eliminated in the distributed results. At 3 radii out of the disk plane, the observer is completely outside the outermost caustic during the entire passage time of the disturbance. This accounts for the nearly negligible magnitudes seen in Figs. 8a and 8i.

Pressure waveform behavior at other radial locations is very similar to that in Fig. 8, except for the widening illuminated zone evident in Fig. 4 and for the spatial decay of amplitude that occurs with increasing propagation distance. The current theory provides explicit expressions for this decay in the form of the factors h_0 and h_1 of Eq. (26) that are not available from the results in Ref. 4. The decay factors are directly associated with the geometric properties of the propagating Mach surfaces. If the expressions for $h(\sigma, \pm B^{1/2})$ are used in Eq. (26), it is found that the overall spatial decay rate varies across the illuminated region, occurring as $R^{-1/2}$ near its center and increasing to R^{-1} near the boundaries of the acoustic shadow.

Acknowledgments

The work was supported by NASA under Cooperative Agreement NCC1-14. The authors thank F. Farassat and M. H. Dunn for their many contributions to this effort.

References

[1]Myers, M. K., and Farassat, F., "Structure and Propagation of Supersonic Singularities from Helicoidal Sources," AIAA Paper 87-7627, Oct. 1987.

[2]Farassat, F., Dunn, M. H., and Padula, S. L., "Advanced Turboprop Noise Prediction Based on Recent Theoretical Results," *Journal of Sound and Vibration*, Vol. 119, No. 1, 1987, pp. 53–79.

[3]Ffowcs Williams, J. E., and Hawkings, D. L., "Sound Generation by Turbulence and Surfaces in Arbitrary Motion," *Philosophical Transactions of the Royal Society of London*, Vol. A264, No. 1151, 1969, pp. 321-342.

[4]Dunn, M. H., and Tarkenton, G. M., "User's Manual for the Langley High Speed Propeller Noise Prediction Program (DFP-ATP)," NASA CR NAS1-1800, Oct. 1988.

[5]Hanson, D. B., "Near-Field Frequency-Domain Theory for Propeller Noise," AIAA Paper 83-0688, April 1983.

[6]Farassat, F., "Advanced Theoretical Treatment of Propeller Noise," von Karman Inst. Lecture Series 81-8210, Brussels, Belgium, May 1982.

[7]Kanwal, R. P., *Generalized Functions—Theory and Technique*, Academic, New York, 1983.

[8]Gel'fand, I. M., and Shilov, G. E., *Generalized Functions, Vol. 1: Properties and Operations,* Academic, New York, 1964.

[9]Wydeven, R., "Advanced Propeller Noise Prediction Employing an Asymptotic Wavefront Approximation," M. S. Thesis, Joint Inst. for Advancement of Flight Sciences, George Washington Univ., Hampton, VA, Dec. 1988.